

Towards a wearable near infrared spectroscopic probe for monitoring concentrations of multiple chromophores in biological tissue in vivo

Danial Chitnis,¹ Dimitrios Airantzis,¹ David Highton,² Rhys Williams,¹ Phong Phan,¹ Vasiliki Giagka,¹ Samuel Powell,¹ Robert J. Cooper,¹ Ilias Tachtsidis,¹ Martin Smith,² Clare E. Elwell,¹ Jeremy C. Hebden,¹ and Nicholas Everdell¹

¹ Department of Medical Physics & Biomedical Engineering, University College London, London WC1E 6BT, UK.

² Neurocritical Care Unit, National Hospital for Neurology and Neurosurgery, University College London Hospitals, London WC1N 3BG, UK.

Abstract

The first wearable multi-wavelength technology for functional near-infrared spectroscopy has been developed, based on a custom-built 8-wavelength LED source. A lightweight fibreless probe is designed to monitor changes in the concentrations of multiple absorbers (chromophores) in biological tissue, the most dominant of which at near-infrared wavelengths are oxyhemoglobin and deoxyhemoglobin. The use of multiple wavelengths enables signals due to the less dominant chromophores to be more easily distinguished from those due to hemoglobin, and thus provide more complete and accurate information about tissue oxygenation, hemodynamics and metabolism. The spectroscopic probe employs four photodiode detectors coupled to a four-channel charge-to-digital converter which includes a charge integration amplifier and an analogue-to-digital converter (ADC). Use of two parallel charge integrators per detector enables one to accumulate charge while the other is being read out by the ADC, thus facilitating continuous operation without dead time. The detector system has a dynamic range of about 80 dB. The customized source consists of eight LED dies attached to a 2 mm × 2 mm substrate and encapsulated in UV-cured epoxy resin. Switching between dies is performed every 20 ms, synchronized to the detector integration period to within 100 ns. The spectroscopic probe has been designed to be fully compatible with simultaneous electroencephalography (EEG) measurements. Results are presented from measurements on a phantom and a functional brain activation study on an adult volunteer, and the performance of the spectroscopic probe is

shown to be very similar to that of a benchtop broadband spectroscopy system. The multi-wavelength capabilities and portability of this spectroscopic probe will create significant opportunities for *in vivo* studies in a range of clinical and life science applications.

1. Introduction

Functional neuroimaging aims to quantify regional brain activity and has found a wide range of applications from cognitive neuroscience to assessment of brain pathology.^{1,2} While functional magnetic resonance imaging (fMRI) and positron emission tomography (PET) provide good spatial resolution and have become established techniques for many applications, both are expensive, cumbersome, and can only be employed within specialist clinical facilities. Applications which require subjects to interact within a natural environment (e.g. developmental psychology studies of children) demand portable technologies, combined with a capacity to monitor multiple cerebral regions of interest and with a higher temporal resolution than that typically achieved using either fMRI or PET. Electroencephalography (EEG), which measures electrical potentials on the scalp resulting from underlying neuronal activity, offers both excellent portability and temporal resolution (~ 1 millisecond) but is severely limited in its ability to spatially localize cortical event related potentials. Functional NIRS (fNIRS) is a non-invasive technique which utilizes measurements on the scalp of the attenuation of near infrared light (700 nm-1000 nm) to characterize the concentrations and oxygenation status of light-absorbing substances (chromophores) in tissue that can change their concentration during brain activation, specifically oxyhemoglobin (HbO₂), deoxyhemoglobin (HHb), and oxidized cytochrome c oxidase (oxCCO).³ Compared to EEG, fNIRS offers complementary information on the vascular and metabolic response to brain activity, has comparable portability, and achieves significantly better spatial resolution (on the order of centimeters), with somewhat inferior temporal resolution (~100 milliseconds).^{3,4,5}

The principal objective of the work described here is the realization of a wearable device for simultaneous NIRS and EEG monitoring of neurovascular and metabolic physiology. During the past twenty years there has been increasing focus on functional imaging with NIRS using multiple near-infrared sources and detectors.⁴ Almost all systems have employed sources at just two discrete wavelengths in order to resolve changes in oxyhemoglobin concentration [HbO₂] and deoxyhemoglobin concentration [HHb]. The

systems typically involve coupling large arrays of optical fibers or fiber bundles to the scalp. Imaging over an entire adult scalp typically requires around 30 discrete source positions and a similar number of detector positions, which often results in an array that is bulky and heavy, and that severely restricts movement. More recently, portable systems have been developed which employ sources and detectors in direct contact with the scalp, with the analogue signal being transferred via long electrical cables to a controller module.^{6,7,8,9} A potential problem with this approach is that long cables can introduce noise into the measurement, although this can be overcome by placing the acquisition electronics adjacent to the sources and detectors on the scalp.¹⁰ Recently, von Lühmann *et al.*¹¹ described a fibreless NIRS system for brain computer interface (BCI) applications where four dual-wavelength sources and a detector comprise a wearable module. Several fibreless NIRS systems are now available commercially. The imaging array provided by Biopac Systems Inc. (Goleta CA, USA) is designed to measure blood oxygenation changes in the prefrontal cortex, as is that developed by Hitachi Medical Corp. (Tokyo, Japan).⁶ The OctaMon system developed by Artinis Medical Systems (Elst, Netherlands) is a lightweight and fully wireless 8-channel NIRS system. TechEn Inc. (Milford MA, USA) have also announced a wearable, wireless system for functional NIRS measurements, while another wearable system which can support up to 16 sources and 16 detectors has been developed by NIRx Medical Technologies (Glen Head NY, USA).

In the sections below we first describe the design and construction of a fibreless multi-wavelength probe for fNIRS, and then report on a demonstration of its performance on a simple tissue-equivalent phantom. Finally, we describe an attempt to simultaneously measure [HHb], [HbO₂], and oxidized cytochrome-c-oxidase (oxCCO) during a functional stimulation study performed on an adult volunteer.

2. Hardware development

a) Design criteria

A major emphasis of the design is that the device should be sufficiently portable and lightweight to eventually enable multiple probes to be combined within an array to facilitate imaging over the entire scalp while allowing the subject to move relatively freely within a normal environment. The device must also be fully compatible with EEG, with an ultimate objective of directly incorporating EEG electrodes in the probe. Resolving simultaneous changes occurring in concentrations of multiple chromophores requires an appropriate multi-wavelength source, where the number of wavelengths is at least as large as the number of

chromophores. Following the analysis by Arifer *et al.*¹² which examined the optimal number of wavelengths to be able to quantify changes in oxCCO, we designed and built our own 8-wavelength light-emitting diode (LED) device. Many existing NIRS imaging systems rely on avalanche photodiodes (APDs) to achieve a high detection gain.^{6,10,13} However, these need to be biased at relatively high voltages (~ 200 V), which is potentially hazardous when placed adjacent to the skin, and they are generally more expensive than conventional photodiodes. To address the limitations presented by many previous systems, we present a probe which incorporates photodiode detectors employed in combination with charge integration amplifiers.

b) *System description*

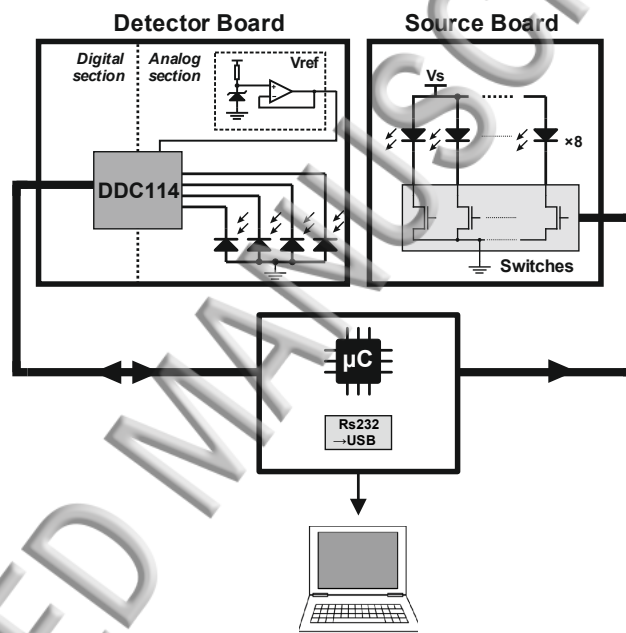


Fig. 1: A schematic diagram of the multi-wavelength NIRS system.

Figure 1 shows a schematic diagram of our portable multi-wavelength NIRS system, which consists of three principal components: a source printed circuit board (PCB), a detector PCB, and a controller. The source board houses a custom-built eight-wavelength LED and its associated driver circuitry. Switching between wavelengths is facilitated using an 8-line digital bus. The detector board consists of four Hamamatsu S12158-01CT photodiodes (7.7 mm^2 photosensitive area) and a four-channel charge-to-digital converter (Texas Instruments DDC114). The photodiodes are directly connected to the high impedance analogue inputs of the DDC114 which includes a charge integration amplifier and a 20-bit Delta-Sigma analogue-to-digital converter (ADC). The integration of the charge amplifier and the ADC within a single

silicon substrate leads to a superior signal-to-noise ratio (SNR) when compared with the use of discrete elements, as each element can be optimized within the integrated circuit. The DDC114 employs two independent charge integrators with a common input for each channel. While one integrator is accumulating the charge from the input, the accumulated charge from the other integrator is converted into digital data by the ADC. This enables continuous operation without any dead time. A square waveform is generated by the controller, and the rising and falling edges of the pulse determine the start and end times of the integration for each channel. The data from all four channels are then transferred to the controller by means of a synchronous serial communication protocol.

The output values of the DDC114 are expressed as the ratio of the accumulated charge to the full scale range of the integration capacitor (Q) in parts per million (PPM). Thus the equivalent current for a constant charge readout is

$$I_{eq} = (\text{PPM} / 1 \times 10^6) \times Q / T , \quad (1)$$

where PPM is the readout value, Q is the full scale charge, and T is the integration time. The largest full scale range, 350 pC, is used for this system. The equivalent trans-impedance gain of the charge integrator can be defined as the ratio between the saturation voltage of the internal op-amp (equal to the 4.096V reference voltage) and the maximum readout value of the DDC114. Hence, using Eq. (1):

$$V_{out}/I_{in} = V_{REF}/I_{eq(max)} = 4.096 \text{ V} / (350 \text{ pC} / 20 \text{ ms}) \approx 200 \text{ MV/A} . \quad (2)$$

The internal noise of the detector module only depends on the noise of the operational amplifiers which means that this noise is independent of the integration time. However, in practice the overall noise of the system is dominated by external interference, which includes that due to 50 Hz mains power (in the UK), and fast switching digital signals in the proximity of the photodetector. The effect of mains power interference can be minimized by setting the integration time to multiples of the period of the waveform (20 ms), which ensures that a complete cycle of the signal appears within a single integration period. However, the mains frequency varies slightly over time, so a lower frequency noise will still appear as a result of aliasing between the mains and internal clock frequencies. The overall noise measured with the detector module is approximately 100 ppm rms, which implies that the detector system has a dynamic range of 80 dB (i.e. four decades of intensity).

The interference from the fast switching digital signals in the proximity of the high impedance analogue inputs of the DDC114 is not observable due to the fast transition between each logic level, which typically occurs in less than 50 ns, faster than the limited frequency response of the DDC114.

Another potential source of interference in the system is timing cross talk occurring at the transitions between individual LED illuminations.

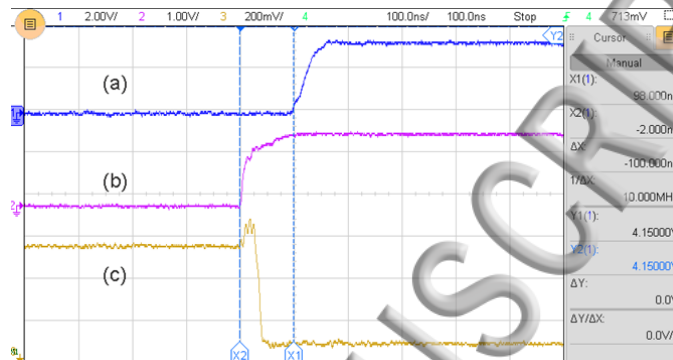


Fig. 2: The transient signals observed during switching of the LEDs

(volt/div a = 2V, b = 1V, c = 0.2V; time/div = 100ns).

Switching between LEDs is intended to occur at the start of each integration period. Figure 2 shows the measured transient signals during an LED switch. Signal (a) shows the rising edge of the square pulse generated by the controller which indicates the start of a new integration time. Signal (b) shows the signal sent from the controller to the LED driver, and signal (c) is the voltage across the LED's cathode. Since the anode of the LED is connected to the positive supply voltage, a negative going voltage at the cathode switches on the LED. These signals suggest that the transition of the LED occurs 100 ns before the new integration begins. Hence, there is 100 ns of cross-talk between one LED and the next. However, the overall effect of the cross-talk is at most 5 ppm ($100 \text{ ns} / 20 \text{ ms}$), which is smaller than the system noise. This cross-talk will be reduced in the future with a dedicated hardware logic to ensure better synchronization is achieved between the integration and the LED signals.

The temperature dependent drift specified for the DDC114 is $\pm 0.5 \text{ ppm per } ^\circ\text{C}$, and the range drift (saturation limit) is $25 \text{ ppm per } ^\circ\text{C}$. Therefore a 10°C temperature increase will result in a 5 ppm change in the offset which is much smaller than the noise of the system (100 ppm). In addition, the range will increase by 250 ppm leading to a relative change of $(250/1,000,000) = 0.025\%$ in the measurement. Moreover, the typical long term offset drift of the DDC114 is specified as only $\pm 0.2 \text{ ppm per minute}$.

c) Source assembly

When determining physiological parameters from NIRS measurements of tissue at multiple wavelengths, it is normally necessary to assume that the measurements sample the same volume of tissue.¹⁴ When using sources at discrete wavelengths, this requires that sources at different wavelengths are co-located as closely as possible. The challenge when developing a multi-wavelength LED source is for the separation between LEDs to be negligible compared to the distances between sources and detectors (typically a few cm). Although off-the-shelf packaged LEDs are available, the large combined footprint of eight individually packaged LEDs would create significant errors in the derived parameters. Thus to minimize the source dimensions, a custom-built device was developed, where eight LED dies were encapsulated within a single package. Each die is a near-infrared AlGaAs semiconductor pn-junction (OSA-Opto, Berlin). The ratio between Al, Ga, and the other dopants varies the bandgap energy of the material, hence determining the emission wavelength of the LED die.¹⁵

Figure 3a shows the prototype device. Each LED die is approximately $350\ \mu\text{m} \times 350\ \mu\text{m}$, with a typical optical power of 5 mW. The dies have the *n*-side (cathode) of the LED facing upwards, while their opposite *p*-side (anode) is metallized for adhesion to the substrate. All the dies are attached to a square gold-coated substrate with dimensions of $2\ \text{mm} \times 2\ \text{mm}$. This area is used as the common anode, so that each die can be individually addressed by passing a current through its cathode. Initially, the substrate is coated with a thin layer of Polytech EC 101 which is a thermally curable conductive paste. The paste creates an electrical connection for the rear surface (anode) of the dies and provides mechanical fixation once it is cured.

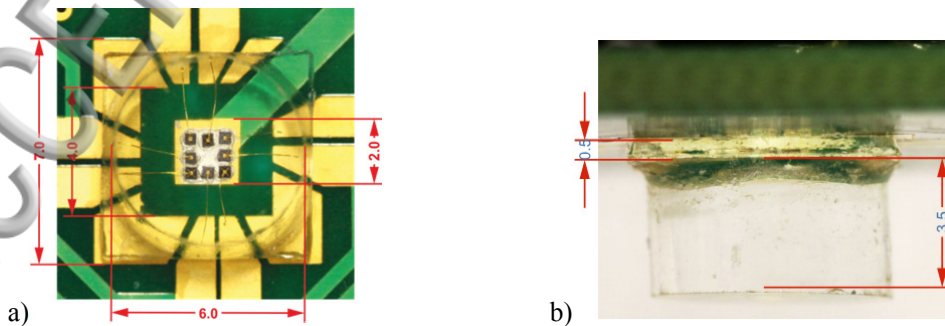


Fig. 3: The multi wavelength LED source and the optical interface. a) top view (b) side view.

The paste is normally applied using a metal stencil, but this leaves a gap between the stencil and the substrate. Due to the low surface tension of the paste a laser-cut adhesive tape was used instead of the metal stencil ensuring that the conductive paste does not spill outside of the designated area, leading to an increased risk of a short circuit between the anode and cathode. The dies were positioned with a placement accuracy of 25 μm using a Finetech Fineplacer vacuum pick and place device, which provides the operator with superimposed images of the substrate and rear surface of the die. Once the dies were mechanically secured on the substrate, the top of each LED was wire bonded to the pads on the source board using a thermosonic ball bonder (Model 4524, Kulicke & Soffa Industries, Inc.). The bonding was performed using a 30 μm diameter gold wire (AW-7, Kulicke & Soffa Industries, Inc.), and a capillary made from toughened alumina (KS-41488-C210-R24, Kulicke & Soffa Industries, Inc.) with a 90° inner cone angle, which produces bonds with a 74 – 102 μm diameter.

To prevent mechanical damage due to the fragility of the wire bonds, the dies were encapsulated in an optically transparent UV-curing epoxy resin. Initially a silicone rubber mask is made to create a cavity for dispensing the liquid epoxy. Since silicone rubber is inherently hydrophobic, a chemical bond to the epoxy resin is prevented and the mask is easily removed when the epoxy is fully cured. The mask was produced using an open cast mold made out of 0.5 mm thick laser-cut acrylonitrile butadiene styrene (ABS). The mold was lightly sprayed with a releasing agent before the platinum cure silicone (Dragon-skin 30, Smooth-On, Inc.) was poured in.

The size of the mask cavity was 7 mm \times 7 mm which allows space for the wire bonds and ensures that they are not damaged when the cavity was filled with UV curing epoxy resin (Norland 81). This has a viscosity of 300 mPas. A low viscosity resin was selected to minimize the likelihood of trapping bubbles (although the uncured resin could be removed with a syringe should bubbles be observed). A drawback of using low viscosity resin is the tendency for it to flow beneath the silicone mask at the edge of the cavity before it is fully cured. This was avoided by inserting drops of higher viscosity resin (Norland 68), which has a viscosity of 5000 mPas, into the edges of the cavity, which is partially cured using a 1mW 365nm UV LED before the cavity is filled with the low viscosity resin. Finally, the cavity was irradiated with the UV LED to cure, and then the silicone mask was removed.

Following encapsulation, short cylindrical light guides were attached to the top surfaces of the photodiode detectors and encapsulated sources in order to provide a channel for the light to travel between the probe and the scalp, bypassing the hair as necessary.^{6,8} Poly Methyl Methacrylate (PMMA) light guides were initially tested, but the optical quality was observed to degrade as a result of contact with Isopropyl Alcohol. Since the guides will be regularly exposed to similar solvents during cleaning, glass light guides were employed instead. A borosilicate glass rod of 6.0 mm diameter was cut into lengths of 3.5 mm. Cutting involved scoring the rod around its circumference with a diamond-tipped blade, and then momentarily placing the end of another rod heated to a molten temperature in contact with the scored line which had been wetted with a drop of water, which causes the rod to break cleanly. One end of the short light guide was then polished (with a sequence of 30, 12, and 0.3 μm aluminum oxide papers) as required to achieve a flat surface of acceptable optical quality. The other end was coupled to the encapsulated LED source using an optical grade UV cured adhesive.

d) *Device construction*

Figure 4a shows the fully assembled source and detector boards, supporting one 8-wavelength source on the left and four photodiode detectors on the right. The center-to-center source-detector separations are 36 mm and 42 mm. The combination of a source with multiple detectors provides measurements sensitive to different depths within the tissue, and facilitates spatially resolved NIRS and imaging methods to improve quantitation of tissue parameters.¹⁶ The two boards are mechanically coupled a pre-determined distance apart within a flexible casing (figures 4b and 4c), which was 3D printed using a Stratasys Objet Connex 500 using a soft rubber-like material Stratasys TangoBlackPlus FLX980, which has a Shore A hardness of 26.

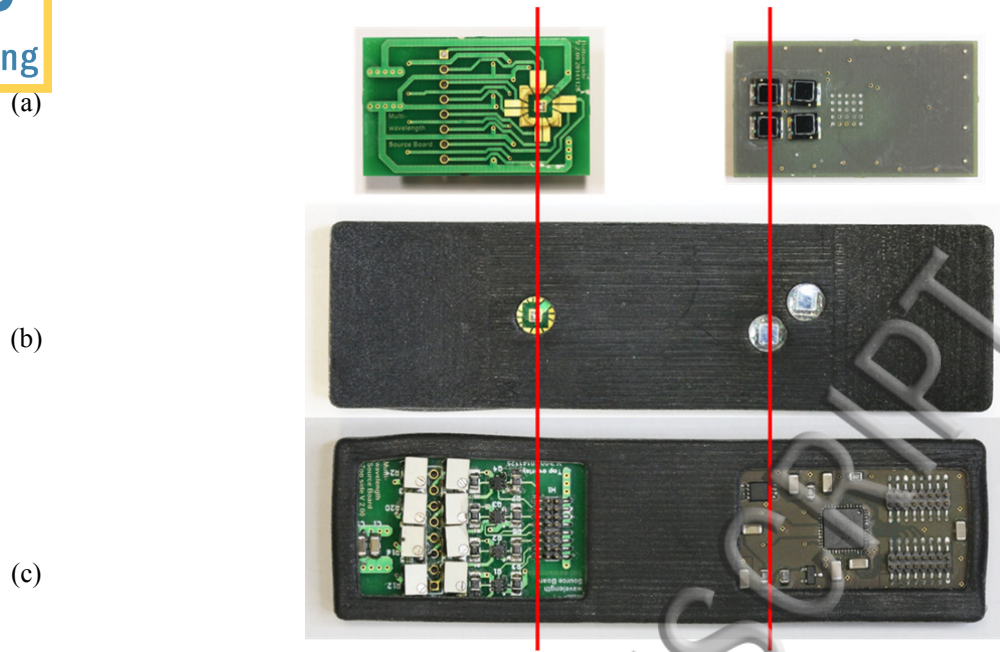


Fig. 4: The assembled NIRS probe. a) The source and detector boards. b) The internal surface of the assembled probe that is in optical contact with the scalp. c) The external surface.

3. System evaluation

a) Initial testing

The data integrity of the system could be affected by erroneous logical operations within the data chain and an inconsistent sampling rate. To verify the integrity of the data between the DDC114 output and the processing software, the response of the detector to an optical sinusoidal signal was investigated. This signal was generated using a red LED with a carefully biased DC operation point so that it operates in the quasi-linear section of the current-voltage characteristic of the LED. At this point the relationship between the applied voltage and the optical power is as linear as possible.¹⁷ This was verified using a digital oscilloscope with a real-time FFT function.

Figure 5a shows the schematic diagram of the circuit that was used to calibrate the sinusoidal signal. An LED was modulated with a combination of a DC bias (V_{DC}) and a sinusoidal signal (V_m). A photodiode was connected in series with a 300k resistor, so that small photocurrent changes were observable as voltage changes across the resistor (V_R) with the oscilloscope, allowing calibration to be performed. The calibrated signal was then applied to the detector board. The DDC114 sends data to the controller which communicates

with the PC via a serial-to-USB bridge. The data were collected and then processed using Matlab (Mathworks, Inc.). Figures 5b and 5c show the received data and the modulus of their Fourier transform respectively. The latter exhibits an intense narrow peak consistent with the sinusoidal input, verifying a high degree of data integrity in the system.

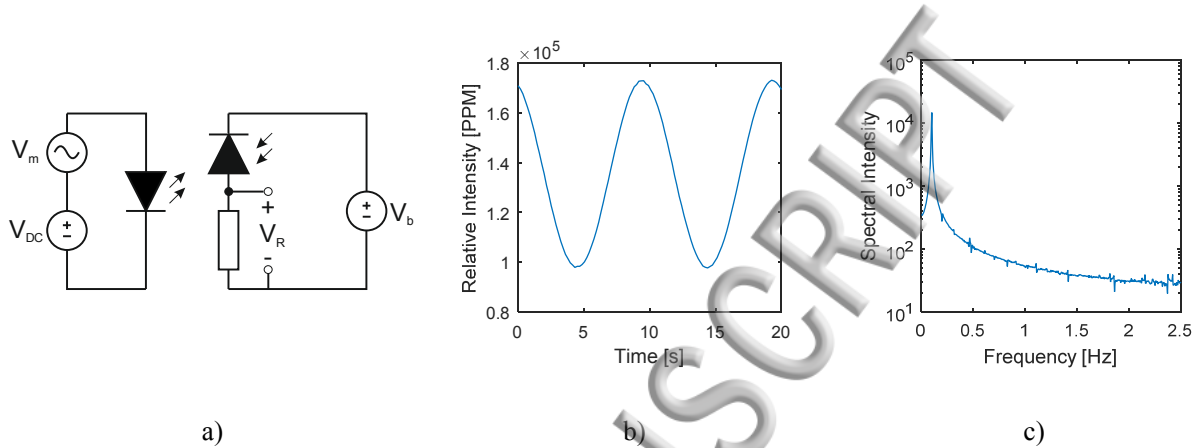


Fig. 5: a) The circuit used for calibration of a red LED employed for data integrity testing of the detector system. b) The sinusoidal signal received by the detector. c) The Fourier transform modulus of the received signal. The peak in the spectral intensity occurs at 0.103 Hz.

The spectral characteristics of each LED within the custom-built 8-wavelength source were measured individually using a benchtop spectrometer, and the results are shown in figure 6. The central wavelengths of the LEDs are spaced over the range 750 nm to 900 nm, and their spectral full-width-half-maximum vary between 30 nm and 50 nm. When first switched on, the variation in source intensity over 10 minutes was never greater than 0.2%. After operating for 30 minutes, the intensity variation (measured at room temperature using a Thorlabs PM100A power meter) was found to be no greater than 0.03%.

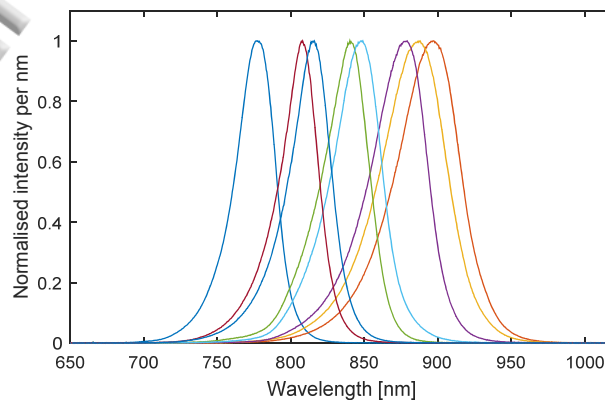


Fig. 6: The spectral characteristics of the eight LEDs. The peaks of the emission spectra occur at wavelengths of 778, 808, 814, 841, 847, 879, 888, and 898 nm.

b) *Evaluation on a tissue-equivalent phantom*

A test of the functionality of the NIRS device was performed using a simple tissue-equivalent phantom illustrated in figure 7. It consists of a solid block of epoxy resin with a cylindrical cavity through which a rod can be manually translated back and forth. The rectangular block (dimensions $95 \times 175 \times 60$ mm) was cast from resin mixed with titanium dioxide particles and dye to provide a transport scattering coefficient of $\mu_s' = 1.0 \text{ mm}^{-1}$ and an absorption coefficient of $\mu_a = 0.01 \text{ mm}^{-1}$ at a wavelength of 800 nm. The absorption coefficient increases linearly by approximately 15% over the wavelength range 750-900 nm. The rod, with a diameter of 10 mm and length of 130 mm, has exactly the same optical properties except for a central “target” region (15 mm in length) which has an absorption coefficient of $\mu_a = 0.1 \text{ mm}^{-1}$. The cavity in the block through which the rod passes is parallel to the top surface, with the center located at a depth of 15 mm. The rod may be translated in order to place the target at any position along the cavity, while the optical properties of the surrounding volume are essentially uniform. A phantom of very similar design was recently developed by Pifferi *et al.*¹⁸ to characterize near-infrared spectroscopy and imaging systems.

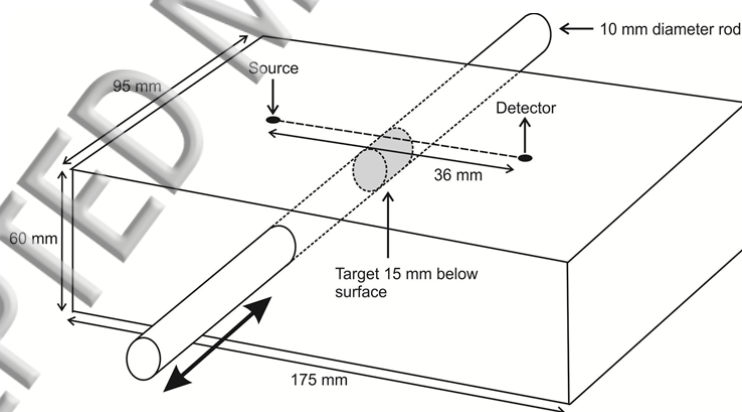
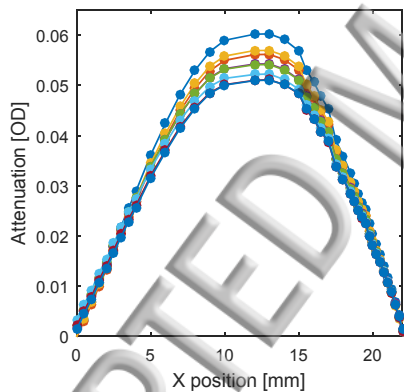


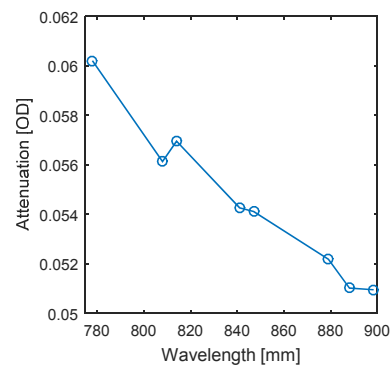
Fig. 7: A solid tissue-equivalent phantom containing a rod which can be manually translated back and forth. The rod incorporates a region with ten times the absorption of the surrounding rod and block.

The probe was positioned on the top surface of the phantom such that a 36 mm line joining the source and the nearest detector was orthogonal to the rod and the midpoint of the line was directly above it (as shown in figure 7). Thus as the target is translated across the center of the cavity, a maximum is observed in the attenuation of light reaching the two detectors from the source. The dark current of each photodiode is

automatically sampled at the start of each LED illumination sequence, and then subtracted from the subsequent intensity measurements. The influence of ambient light was eliminated by wrapping the phantom and probe in black cloth. The variation in attenuation as seen by the nearest detector (36 mm separation) for each of the eight LEDs is shown in figure 8a over a translation range of 22 mm, and the dependency of the maximum change with wavelength is shown in figure 8b. The absolute attenuation between the source and detector is estimated to be about 40-50 dB, and the maximum change in attenuation due to the presence of the target (relative to a homogenous block) is estimated to be about 1-2 dB. While the linear increase in absorption coefficient with wavelength also increases the inherent contrast of the target, the proportion of detected light which reaches the target will decrease with wavelength (longer pathlength photons are more likely to be absorbed than shorter pathlength photons), and this is the dominant effect. The attenuation variation for the furthest detector (42 mm) exhibited a very similar trend (not shown) over a slightly smaller range.



(a)



(b)

Fig. 8: a) The variation in the attenuation of received light for each LED as the high absorbing region of the rod is translated through the midpoint of the cavity in the phantom, below the midpoint of the line joining the source and the detector. b) The observed maximum change in attenuation due to the high absorbing region as a function of wavelength.

c) *A functional brain activation study on a human subject*

The probe was tested on a healthy subject undergoing an ethically-approved visual stimulation paradigm designed to elicit a functional response in the primary visual cortex. The short light guides protrude

a few millimeters below the encapsulation, so that a small circular movement of the probe during placement on the head is sufficient to move the hair away. The probe was then held in place using a strip of self-adherent bandage wrapped around the head. Results were compared with an identical study performed on the same subject using a broadband NIRS system (with continuous spectral coverage over the range 780-900 nm) described by Kolyva *et al.*¹⁹ The visual paradigm required the subject to observe a 4 Hz inverting checkerboard for 20 seconds, followed by 20 seconds observing a blank screen, repeated 20 times. Both systems used a source-detector separation of 36 mm, with the midpoint placed directly over the expected center of the left visual cortex estimated by the 10-20 electrode placement system. Although the portable probe also collected data at the longer 42 mm separation, this was not used for the comparison with the broadband system.

Prior to the experiment, the LED intensities were adjusted so that the signals detected by the nearest photodiode would be approximately equal. This was achieved by placing the probe in contact with the arm of a volunteer, and assuming that the optical properties would be roughly the same as those of a human head. The minimum detected intensity among the 8 wavelengths was 37,500 ppm (corresponding to 1.05 nW; see section 2b above), and the maximum was 95,100 ppm (2.44 nW). At the wavelength with the largest average intensity (89,000 ppm), the stimulus produced an amplitude variation of approximately 13,000 ppm. Thus, using the measured noise level of 100 ppm, the achieved SNR is approximately 59 dB and the contrast-to-noise ratio (CNR) is 42 dB.

The broadband spectrometer acquired measurements at a rate of 1 Hz, and the raw data were high pass filtered with a 5th order Butterworth filter (0.02 Hz) to remove slow baseline drift. Data from the LED based system were band pass filtered (0.02–1 Hz) to remove cardiac pulsation as well. Data acquired by both systems were block averaged over the periods of stimulus and rest, and these were then processed using the UCLn algorithm (as described by Kolyva *et al.*¹⁹) to derive estimates of the average changes in concentrations of HbO₂, HHb, oxidized CCO ($\Delta[\text{HbO}_2]$, $\Delta[\text{HHb}]$, and $\Delta[\text{oxCCO}]$ respectively). Figures 9a and 9b display these changes for the broadband and 8-wavelength systems respectively. The stimulus is applied over the period 0-20 seconds, during which $\Delta[\text{HHb}]$ and $\Delta[\text{HbO}_2]$ show the characteristic hemodynamic response (increase in HbO₂ and decrease in HHb) consistent with an increase in localized

cerebral blood flow following neuronal activation. The changes in the estimated $\Delta[\text{oxCCO}]$ signal are consistent with an increase in metabolic activity during functional activation.

During measurement with both systems, an EEG scalp electrode was placed at the adjacent O2 position (as defined by the 10/20 electrode placement system), with a reference electrode placed at the left pre-auricular point. The purpose is partly to confirm neuronal activation, but also to verify that no interference occurs between the optical and EEG systems that we propose to eventually combine within the device. A continuous wavelet transform was performed (using the CWT Morlet wavelet function in Matlab) over scales 1-150 (pseudofrequency range 2.7 Hz - 416 Hz) from the 512 Hz EEG data. The absolute wavelet coefficients were then also block averaged reflecting the time varying power over this range. Figure 9c shows the average EEG power displayed over the same 40 second period as the optical data. Most EEG power is concentrated within a lower 4 Hz band, corresponding to the frequency of the checkerboard inversion. This is only apparent during the stimulus. A higher 10 Hz (alpha wave) band is also visible, which is more intense when the visual stimulus is absent.

A significant concern when attempting to derive changes in oxCCO from NIRS data is the possibility of the result being influenced by corresponding changes in the concentrations of HHb and HbO₂ (a phenomenon known as parameter crosstalk). This is due to the similarity between the absorption spectrum of HbO₂ and HHb (i.e. the specific extinction coefficients of HbO₂ and HHb as a function of wavelength) and the difference absorption spectrum between the oxidized and reduced forms of CCO.¹⁹ To investigate the likelihood of crosstalk, the UCLn algorithm was also used to derive changes in concentration of HHb and HbO₂ only, and the residual in this two-component fitting process was compared with that obtained for the three-component fit. The residuals (i.e. the changes in optical density not accounted for by the chromophore concentration changes) are shown plotted against the center wavelengths for each of the eight LEDs in figure 9d. The residual of the two-component fit is not only larger, but it has a form which is similar to the difference absorption spectrum between the oxidized and reduced forms of CCO.²⁰ A range of studies have previously been performed with benchtop broadband spectroscopy systems to fully investigate the separation of the HbO₂, HHb and oxCCO signals and to optimize systems for measurement of oxCCO.^{20,21} Studies of this type are required to further investigate the measured oxCCO signal from this probe.

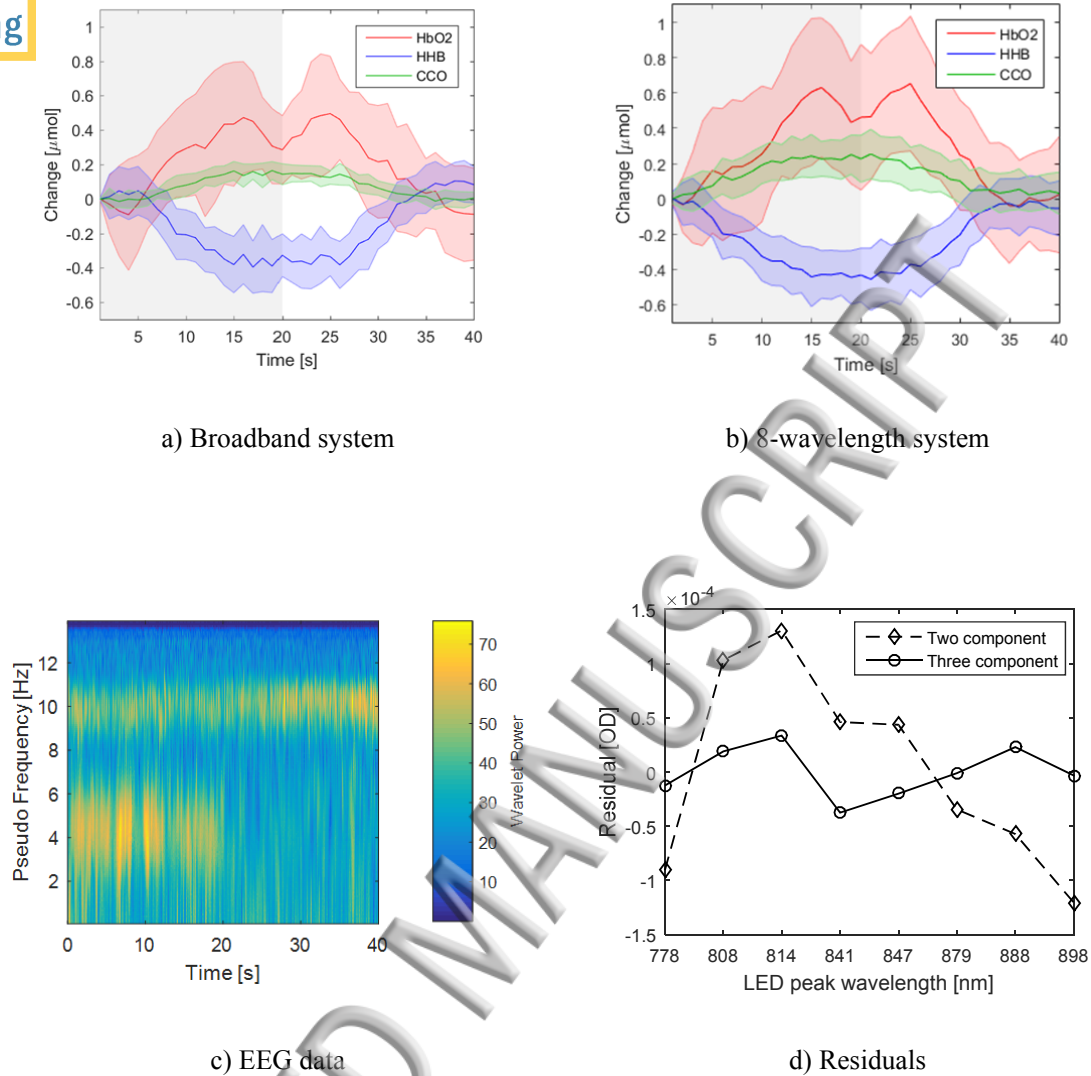


Fig. 9: The results obtained from the visual stimulation paradigm. This shows $\Delta[\text{HbO}_2]$, $\Delta[\text{HHb}]$, and $\Delta[\text{oxCCO}]$ derived from the block averaged broadband (a) and (b) 8-wavelength data. The average EEG data recorded over the same interval is shown in (c), and the residuals obtained from a 2-component and 3-component fit to the data acquired with the 8-wavelength system are shown in (d).

4. Discussion

The prototype device described above succeeded in meeting all the initial design criteria, including portability, use of lightweight components, and compatibility with EEG. The greatest technical challenge was generating the 8-wavelength source, as no commercial package was suitable. Co-locating the eight LED dies as closely as possible was important in order that an assumption can be made that the volumes of tissue sampled at each wavelength coincide, a necessary condition for deriving accurate estimates of tissue

properties.¹⁴ The design achieved co-location to within 1-2 mm, an almost negligible variation compared to the 36 mm center-to-center source-detector separation, and corresponding to an area significantly smaller than that of the photodiode detectors (7.7 mm^2). The novel design of the detector electronics, employing integrated charge integration amplifiers and ADCs, achieved a dynamic range of 80 dB, sufficient to acquire measurements continuously without dead time and over a broad range of source-detector separations simultaneously. The physical characteristics and data acquisition parameters of the system are summarized in Table 1.

ACCEPTED MANUSCRIPT

Parameter	Value
Dimensions of the detector board	38 × 21 mm
Dimensions of the source board	38 × 23 mm
Size of the module holder	103 × 30 × 10 mm
Integration time	20 ms
Number of wavelengths	8
Sampling rate	5.56 Hz
Source-detector separations	36 mm and 42 mm
Dynamic range	80 dB
Resolution	20 bits
Maximum SNR	> 40 dB

Table 1: Summary of physical characteristics and data acquisition parameters.

The multi-wavelength capabilities of this new probe make possible the measurement of oxCCO in addition to the hemoglobin based markers of tissue oxygenation. Changes in oxCCO may be closely localized to regions of brain activity,²² offering potential advantages over hemoglobin based measures which are prone to contamination from extracerebral tissues. Only CCO oxidation changes can give a direct indication of metabolic activity, and this is particularly valuable in cases of brain injury where abnormalities of neurovascular coupling are frequently encountered.² Although this broadband technique enables measurements to be made at more than 100 discrete wavelengths of light, recently we have demonstrated that optimization to 5-8 wavelengths appears to be feasible,¹² and this offers considerable potential for transition to alternative hardware platforms such as those described in this paper. Until now, almost all published *in vivo* measurements of oxCCO have been performed using benchtop broadband spectrometers. No current commercial NIRS systems are designed to measure CCO, although the Hamamatsu NIRO 300 spectrometer released in 1998 did offer this facility.²³ The advent of a wearable spectroscopic probe will enable oxCCO to be measured in a range of clinical and life science scenarios. Further work is required to evaluate in more detail the performance of the LED device with respect to multi-chromophore measurements and the CCO measurement across a range of experimental paradigms. However, the presented hardware shows considerable promise as a scalable component in a multi-source multi-detector imaging system that can be used for this evaluation.

Work is ongoing to increase both the performance and wearability of the device. We are developing means of protecting the components from the static electrical charge generated by the module holder and the glass rods when they are in contact with the scalp. An electrostatic discharge event can permanently damage the sensitive components within the module. Hardware and software solutions are being explored to further reduce the effect of the 50 Hz mains noise affecting the system. This will lead to a lower noise floor and increased dynamic range, enabling the system to employ larger source-detector separations and be more tolerant of light loss, e.g. that caused by the presence of thick dark hair on the scalp. Other planned improvements include a rechargeable power source and a wireless data transfer system, as already demonstrated for other wearable NIRS devices,^{6,7,9,10,13} and integration with a suitable EEG system.¹⁰

Finally, we are developing means of increasing the compactness of the system to enable multiple sources and detectors to be combined in an array to facilitate functional neuroimaging. This will require synchronizing the control of multiple units. The choice of detector obviates the use of frequency modulation, so imaging must necessarily use a combination of temporal multiplexing (illuminating sources in sequence) and spatial multiplexing (illuminating sufficiently separated sources simultaneously). Achieving the most efficient combination is thus reduced to a numerical optimization problem, which can be adapted for a specific array configuration and tissue optical properties. Implementation schemes are currently under development.

Acknowledgments

This work has been funded by the EPSRC (EP/K020315/1 and EP/J021318/1) and by the Department of Health's National Institute for Health Research Centres funding scheme via the UCLH/UCL Biomedical Research Centre. IT is supported by the Wellcome Trust (088429/Z/09/Z and 104580/Z/14/Z).

References

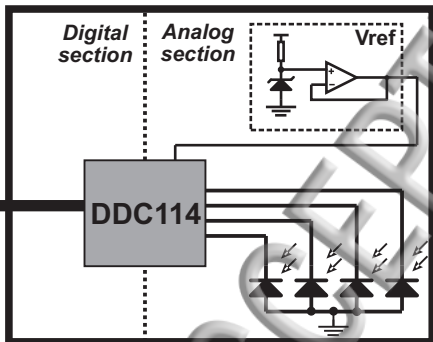
- ¹ R. Cabeza, and L. Nyberg, "Imaging cognition II: An empirical review of 275 PET and fMRI studies".
Journal of Cognitive Neuroscience, 12(1), 1–47, (2000).
- ² E. M. C. Hillman, "Coupling mechanism and significance of the BOLD signal: a status report". Annual
Review of Neuroscience, 37, 161–181, (2014).
- ³ A. Ghosh, C. Elwell, and M. Smith, "Review article: cerebral near-infrared spectroscopy in adults: a work
in progress", *Anesthesia and Analgesia*, 115(6), 1373–1383, (2012).
- ⁴ M. Ferrari, and V. Quaresima, "A brief review on the history of human functional near-infrared
spectroscopy (fNIRS) development and fields of application", *Neuroimage*, (2012).
- ⁵ F. Scholkmann, S. Kleiser, A. J. Metz, R. Zimmerman, J. M. Pavia, U. Wolf, and M. Wolf, "A review on
continuous wave functional near-infrared spectroscopy and imaging instrumentation and methodology,"
Neuroimage 85, 6-27 (2014).
- ⁶ M. Kiguchi, H. Atsumori, I. Fukasaku, Y. Kumagai, T. Funane, A. Maki, Y. Kasai, and A. Ninomiya,
"Note: Wearable near-infrared spectroscopy imager for haired region", *Review of Scientific Instruments*,
83, (2012).
- ⁷ J. Safaie, R. Grebe, H. Abrishami Moghaddam, and F. Wallois. "Toward a fully integrated wireless
wearable EEG-NIRS bimodal acquisition system." *Journal of neural engineering* 10, no. 5 (2013)
- ⁸ S.K. Piper, A. Krueger, S. P. Koch, J. Mehnert, C. Habermehl, J. Steinbrink, H. Obrig, and C. H. Schmitz.
"A wearable multi-channel fNIRS system for brain imaging in freely moving subjects." *Neuroimage*, 85,
64-71, (2014)
- ⁹ R. McKendrick, R. Parasuraman, and H. Ayaz. "Wearable functional near infrared spectroscopy (fNIRS)
and transcranial direct current stimulation (tDCS): expanding vistas for neurocognitive augmentation."
Frontiers in systems neuroscience, 9, (2015).
- ¹⁰ M. Sawa, M. Tariqus Salam, J. Le Lan, A. Kassab, S. Gélinas, P. Vannasing, F. Lesage, M. Lassonde,
and D. Khoa Nguyen, "Wireless recording systems: From noninvasive EEG-NIRS to invasive EEG
devices", *IEEE Transactions on Biomedical Circuits and Systems*, 7, no. 2, 186-195, (2013).

- ¹¹ A. von Lühmann, C. Herff, D. Heger, and T. Schultz, “Towards a wireless open source instrument: functional near-infrared spectroscopy in mobile neuroergonomics and BCI applications,” *Frontiers in Human Neuroscience* 9:617 (2015).
- ¹² D. Arifler, T. Zhu, S. Madaan, and I. Tachtsidis, “Optimal wavelength combinations for near-infrared spectroscopic monitoring of changes in brain tissue hemoglobin and cytochrome c oxidase concentrations.” *Biomedical Optics Express*, 6(3), 933–947, (2015)
- ¹³ J. Si, R. Zhao, Y. Zhang, N. Zuo, X. Zhang, and T. Jiang. “A portable fNIRS system with eight channels”, *Optical Techniques in Neurosurgery, Neurophotonics and Optogenetics*, SPIE, 9305, (2015).
- ¹⁴ T. Correia, A. P. Gibson, and J. C. Hebden, “Identification of the optimal wavelengths for optical topography: a photon measurement density function analysis”, *Journal of Biomedical Optics*, 15, 056002, (2010).
- ¹⁵ R. Pratesi, “Diode lasers in photomedicine”, *IEEE Journal of Quantum Electronics*, 20, 12, 1433, (1984).
- ¹⁶ S. TS. Suzuki, T. Ozaki, and Y. Kobayashi, “A tissue oxygenation monitor using NIR spatially resolved spectroscopy”, *Proc Soc Photo Opt Instrum Eng*, 3597, 582, (1999).
- ¹⁷ H. Elgala, R. Mesleh, and H. Haas, “A study of LED nonlinearity effects on optical wireless transmission using OFDM”, *IFIP International Conference on Wireless and Optical Communications Networks*, 1, 5, 28, (2009).
- ¹⁸ A. Pifferi, A. Torricelli, R. Cubeddu, G. Quarto, R. Re, S. K. V. Sekar, L. Spinelli, A. Farina, F. Martelli, and H. Wabnitz, “Mechanically switchable solid inhomogeneous phantom for performance tests in diffuse imaging and spectroscopy,” *J. Biomed. Opt.* 20(12), 121304 (2015).
- ¹⁹ C. Kolyva, A. Ghosh, I. Tachtsidis, D. Highton, C.E. Cooper, M. Smith, and C. E. Elwell, “Cytochrome c oxidase response to changes in cerebral oxygen delivery in the adult brain shows higher brain-specificity than haemoglobin”, 85(0), 234–244, (2014)
- ²⁰ G. Bale, S. Mitra, J. Meek, N. Robertson, and I. Tachtsidis. “A new broadband near-infrared spectroscopy system for in-vivo measurements of cerebral cytochrome-c-oxidase changes in neonatal brain injury”, *Biomedical Optics Express*, 5, 3450, (2014)
- ²¹ A. Bainbridge, I. Tachtsidis, S. D. Faulkner, D. Price, T. Zhu, and E. Baer, “Brain mitochondrial oxidative metabolism during and after cerebral hypoxia-ischemia studied by simultaneous phosphorus magnetic-

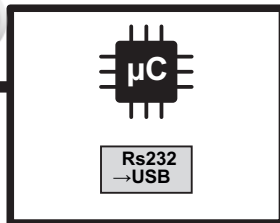
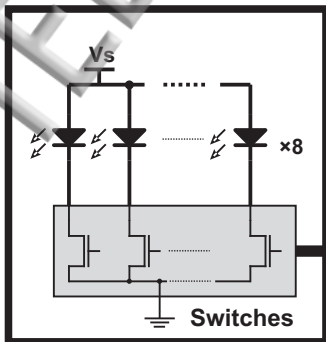
- resonance and broadband near-infrared spectroscopy”, *NeuroImage*, 102 , 173, (2014)
- ²² H. R. Heekeren, M. Kohl, H. Obrig, R. Wenzel, W. von Pannwitz, S. J. Matcher, U. Dirnagl, C. E. Cooper, and A. Villringer. “Noninvasive assessment of changes in cytochrome-c oxidase oxidation in human subjects during visual stimulation.” *Journal of Cerebral Blood Flow & Metabolism*, 19, 6, 592, (1999).
- ²³ M. Thavasoathy, M. Broadhead, C. Elwell, N. Peters, and M. Smith, “A comparison of cerebral oxygenation as measured by the NIRO 300 and the INVOS 5100 Near-Infrared Spectrophotometers”, *Anaesthesia*, 57, 999, (2002).

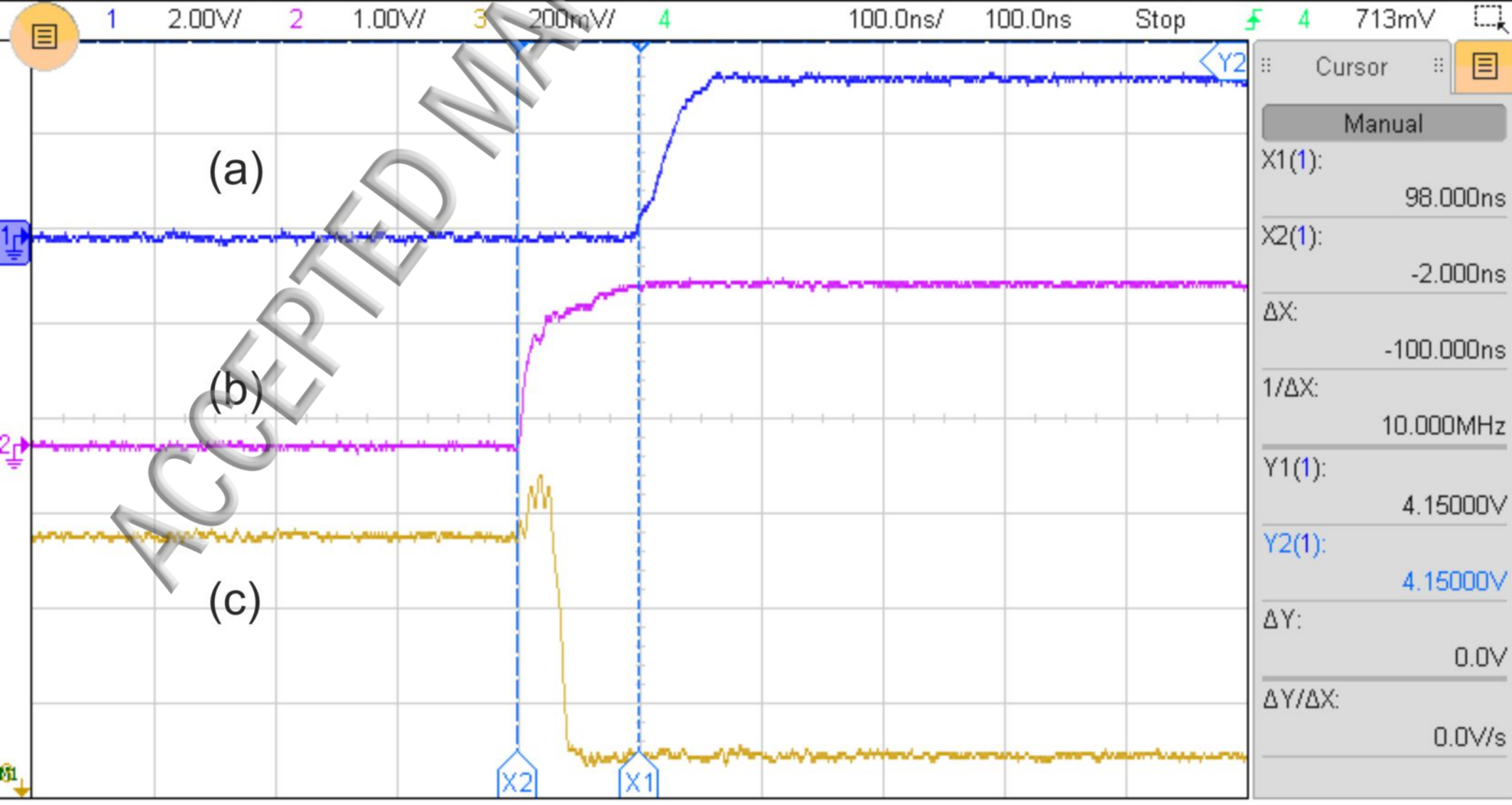
ACCEPTED MANUSCRIPT

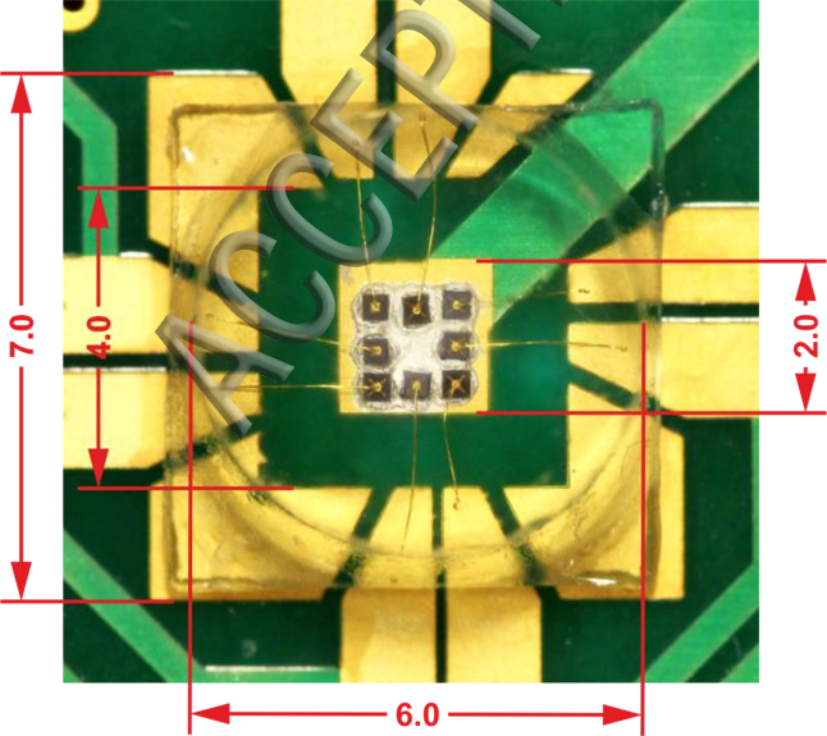
Detector Board

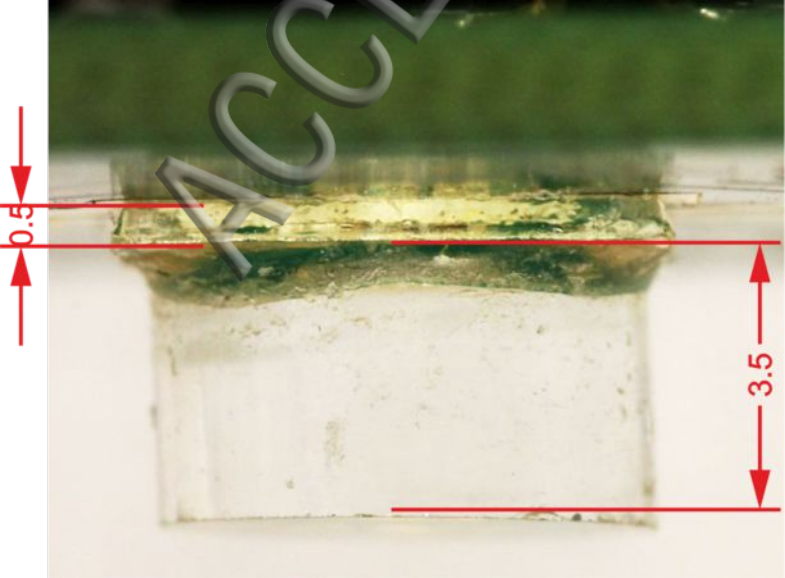


Source Board

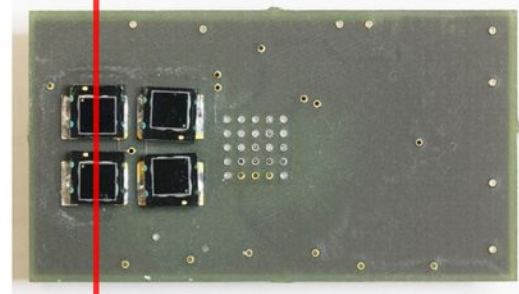
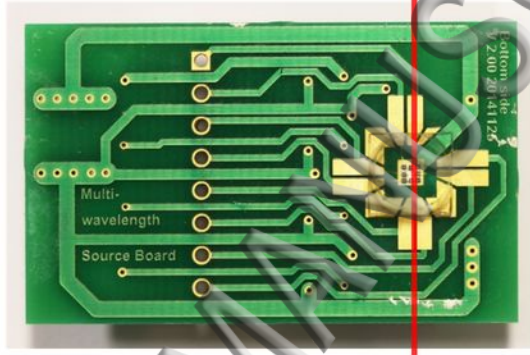








(a)



(b)



(c)

